Nanoscale

PAPER

View Article Online
View Journal | View Issue

Cite this: *Nanoscale*, 2022, **14**, 12022

Tuning spin wave modes in yttrium iron garnet films with stray fields

Ushnish Chaudhuri,[a] Navab Singh,[b] R. Mahendiran *[a] and Adekunle O. Adeyeye *[c,d]

Received 2nd February 2022,
Accepted 22nd July 2022

DOI: 10.1039/d2nr00618a

rsc.li/nanoscale

The nanopatterning of Yttrium Iron Garnets (YIGs) has proven to be a non-trivial problem even with advances in modern lithography techniques due to non-compatibility with a conventional complementary metal oxide semiconductor platform. In an attempt to circumvent this problem, we demonstrate a simple and reliable method to indirectly pattern YIG films on a Gadolinium Gallium Garnet (GGG) substrate. We fabricated exchange-coupled arrays of Py dots onto the underlying YIG films using nanostencil lithography. The stray fields generated from the Py dots were used to transfer patterned magnetic information to the underlying YIG films. The static and dynamic properties of the fabricated hybrid YIG/Py dot structure and reference YIG film were characterized using the focused magneto-optic Kerr effect and by broadband ferromagnetic resonance spectroscopy. For the reference YIG film, as expected, a single field-dependent resonance mode with a narrow linewidth was observed in contrast to the splitting into three distinct resonance modes for the YIG/Py dot structure as predicted by micromagnetic simulations. We have thus shown that it is possible to utilize stray field effects from easily patternable magnetic materials for the development of future YIG-based magnonic devices.

Introduction

Yttrium iron garnets ($Y_3Fe_5O_{12}$, YIGs) and other ferro/ferrimagnetic insulators, which exhibit lower Gilbert damping, are ideal materials for efficient spin-wave propagation over long distances[1,2] High-quality crystalline YIG films have been prepared on lattice-matched substrates such as Gadolinium Gallium Garnets ($Gd_3Ga_5O_{12}$, GGGs)[3] by liquid phase epitaxy (LPE),[4] pulsed laser deposition (PLD),[5] and magnetron sputtering[6,7] using various groups. Moreover, investigations into the properties of YIGs revealed exciting spin-wave properties that can be utilized for various applications in magnonics.[8] Ferromagnetic nanostructures form building blocks in the development of magnonic or spintronic devices. Permalloy ($Ni_{80}Fe_{20}$ alloy, Py) nanostructures have already demonstrated great potential and versatility in developing devices that are used for logic, data storage,[9] and biological sensing.[10] Py and other ferromagnetic metals, however, exhibit plasmon–magnon interactions that heavily damp spin wave propagation through them. Unfortunately, the nanofabrication of YIG-based devices has been difficult due to the high cost of integration of epitaxial YIG films and compatibility issues with the current complementary metal oxide semiconductor technology. Several groups have tried various methods to pattern YIGs. One route involves the ion etching of sputtered YIG films using resist masks to define the patterned structures.[11] However, high energy Ar ions can damage the film quality which may lead to high damping in YIG films.[12] The ion milling of YIG thin films can also change the magnetic properties of the film,[11] making this process less suitable. Another alternate route involves the etching of the GGG substrate itself[13] followed by the sputter deposition of YIG. The most common method to fabricate YIG nanostructures involves electron beam lithography (EBL) and a lift-off process.[14] However, to overcome electron charging effects that make EBL taxing, since high-quality epitaxial YIG films can only be grown on an insulating GGG substrate, a thin gold layer is deposited on the GGG before the electron beam resist is coated, which is followed by high voltage electron exposure and gold etching. Subsequently, the YIG film is deposited by magnetron sputtering followed by a final lift-off process.[15] This multi-stage fabrication process makes EBL expensive and cumbersome. Another interesting technique employed to pattern YIGs on silicon substrates involves the use of anodic alumina oxide (AAO) membranes which are used for masking purposes.[16] This technique, however, is limited to specific geo-

[a]*Physics Department, National University of Singapore, 117551, Singapore. E-mail: phyrm@nus.edu.sg*
[b]*A*STAR Institute of Microelectronics, 2, Fusionopolis Way, 138634, Singapore*
[c]*Department of Electrical and Computer Engineering, National University of Singapore, 117576, Singapore*
[d]*Department of Physics, Durham University, South Rd, Durham, DH1 3LE, UK. E-mail: adekunle.o.adeyeye@durham.ac.uk*

metry and lacks uniformity. High-quality YIG films with gilbert damping less than 10^{-4} can also be grown using liquid phase epitaxy (LPE); however, they are usually above 100 nm thick because the LPE-YIG quality of ultra-thin YIG samples starts to degrade.[17] For ultra-thin YIG films, pulsed laser deposition (PLD) is preferred, however, magnetron sputtering is more compatible with the industry.

To circumvent these problems associated with the nanopatterning of YIG films on GGG substrates, we propose a simple method that involves the use of stray fields to virtually transfer magnetic information from Py dot arrays through exchange coupling to the underlying YIG films. Since spin wave information generated in either layer can be transferred to each other, and local stray fields from the Py structures can alter the propagation of spin waves inside the YIG, various studies have also attempted to tune spin waves in the YIG thin film by depositing a Py layer adjacent to it.[18,19] Py nanostructures on top of the YIG were also previously investigated to demonstrate a microwave magnonic transducer,[20] however, the effects of the stray fields from Py nanostructures have not been investigated. Our fabrication process will make use of resistless nanostencil lithography to deposit high-quality Py dots on YIG films. Compared to conventional nanostructure fabrication processes, which comprise multiple resist processing, depositions and chemical processes, nanostencil lithography is non-destructive which is crucial to prevent any parasitic spin wave excitations due to non-uniformity in edges. To date, stencil lithography has been used to fabricate contacts on graphene since it prevents any surface contaminants during the process.[21] Nanomagnetic logic devices[22] and nanostructured antenna arrays[23] have also been fabricated using stencil lithography.

In this paper, we fabricate hybrid Py nanodot/YIG structures by first depositing a high-quality YIG film on a GGG substrate by magnetron sputtering and a post-deposition annealing process. This was followed by the deposition of Py nanodots using nanostencil lithography.[24] Nanostencil lithography is resistless and requires no prior coating with toxic solvents or prior treatment of the substrate. Nanostencil lithography is a parallel process that can be used to pattern a large area in single-step deposition compared with a multi-level EBL process.[25] In our fabrication process, nanopatterned stencils are placed over the substrates while the material is evaporated in a vacuum chamber. The evaporated material passes through the apertures in the stencils and is deposited on the substrate placed over it. Later, the stencils are removed and can be used again. Micromagnetic simulations were performed to understand both the static and dynamic behavior of the hybrid Py nanodot/YIG structure.

Experimental details

Sample fabrication

20 nm YIG films were sputter-deposited on (111)-oriented gadolinium gallium garnet (Gd3Ga5O12, GGG) single crystal substrates at room temperature (RT) from a commercial YIG sputter target. The partial pressure and sputtering power of the chamber were maintained at 3 mTorr and 150 W respectively, which is the optimal deposition environment for RT growth. The films were subsequently subjected to *ex situ* post-annealing at 800 °C for 12 hours in a furnace. Heating and cooling were performed at 1 °C per minute. After the samples were annealed, XRD and FMR spectroscopy were performed on a sample from the same batch to determine crystallinity and film quality. A stencil membrane with regularly spaced holes was placed on top of the YIG thin film grown on the GGG and Py was evaporated to fabricate the Py dots on the YIG film. The chamber pressure was about 8×10^{-8} Torr during the evaporation process.

FMR measurements

A typical microstrip line FMR setup was used for dynamic magnetization measurements. The sample was placed flipped down on the stripline. The external magnetic field was swept from 5000 Oe to 200 Oe at a constant frequency (f) supplied by a vector network analyzer to generate a dynamic magnetic field. A lock-in detection technique was used to measure the absorbed power (dP/dH) by the sample at discrete frequencies from 2 GHz to 15 GHz.

Simulation details

Micromagnetic simulations at $T = 0$ K using the OOMMF software were performed. We listed the simulation parameters used for the Py and the YIG layers as follows: the saturation magnetization values $M_S^{Py} = 800$ emu cm^{-3} and $M_S^{YIG} = 160$ emu cm^{-3} and the exchange constants $A^{Py} = 13 \times 10^{-7}$ erg cm^{-1} and $A^{YIG} = 4 \times 10^{-7}$ erg cm^{-1}. For both the layers, the magnetocrystalline anisotropy was $K_1 = 0$ erg cm^{-3}. The magnetocrystalline anisotropy of the bulk Py film was assumed to be negligible when compared with the shape anisotropy of the patterned nanodots. The most important parameter for our simulation is the exchange parameter between the YIG and the Py layer which represents the strength of the ferromagnetic interaction between the layers. Periodic boundary conditions were also used. This interaction can be described by a bilinear exchange constant 'J'. For the simulations, we have used $J = 0.18$ erg cm^{-2}.[26] A unit cell size of $5 \times 5 \times 5$ nm^3 was used for simulating the static magnetization. To simulate the magnetization reversal process, the damping coefficients of α for both were taken as 0.5 for rapid convergence. To simulate the dynamic magnetization response, time (t) dependent simulations were performed using a $\sin c$ wave excitation field: $h_{\sin c} = h_0 \frac{((\sin(2\pi f t)))}{t}$, where $h_0 = 50$ Oe, with a gyromagnetic ratio of $\gamma/2\pi = 2.8$ GHz kOe^{-1}. The damping coefficients for YIG and Py were taken as $\alpha^{YIG} = 0.001$ and $\alpha^{Py} = 0.008$. The sinc wave was used in the simulation to obtain uniform excitation in the frequency domain. The dynamic simulation results were analyzed in the frequency domain after Fast Fourier Transform (FFT) processing.

Results and discussion

To fabricate these structures, Py dots were deposited on a 20 nm YIG continuous film using stencil lithography. As shown in Fig. 1a, a membrane with the desired pattern was placed on top of the YIG film grown on the GGG by magnetron sputtering. This membrane allowed only evaporated Py to pass through the nanosized apertures. After removing the membrane, atomic force microscopy (AFM) analysis was performed to measure the surface morphology of the fabricated samples. Regularly spaced dots were observed and are presented in Fig. 1b. The AFM results show Py dots of diameter 500 nm, arranged with a center-to-center distance of 1000 nm. The thickness of the dots was found to be 50 nm. A longitudinal magneto-optical Kerr effect (MOKE) setup was used to obtain a normalized M–H loop from the sample of Py dots on the YIG, as shown in Fig. 1c. The M–H loop shows regions of saturation, nucleation, and vortex which were in good agreement with the simulated results in Fig. 4a. Before deposition, a YIG film grown under the exact conditions was used to characterize the YIG film for its damping and crystallography. The inset in Fig. 1c shows the 2θ scan for the sample. The result reveals the existence of the YIG phase with no other phases, suggesting that the YIG thin film is well crystallized along with the (111) orientation. The ferromagnetic resonance (FMR) spectra were recorded in the frequency range of 2 GHz to 15 GHz and the magnetic field was swept from 200 Oe to 5 kOe and therefore magnetization dynamics were studied only in the saturated region.

In Fig. 2a, the normalized FMR response at 12 GHz from a 20 nm continuous film of the YIG is presented in the top panel, while the response from a 50 nm Py dot array deposited on the GGG is presented in the middle panel and the response from the Py dots grown on the YIG film is presented in the bottom panel. A plot of the resonance frequencies of the continuous YIG film and the two strongest modes observed in the Py dot array on the GGG are shown in Fig. 2b using solid symbols. At 1000 Oe, the resonance of the YIG film occurred at 4.3 GHz while the strongest mode of the Py dots occurred at 8 GHz. The resonance frequencies from the continuous YIG film were analyzed by fitting the data to the Kittel equation:

$$f_r = \gamma/2\pi[(H + (N_z - N_x)4\pi M_x)(H + (N_y - N_x)4\pi M_x)]^{\frac{1}{2}} \quad (1)$$

where M_x is the magnetization along the applied field direction, H is the external applied magnetic field, and N_x, N_y, and N_z are the demagnetizing factors of the area along the X–Y and thickness (Z) directions of the film. γ is the gyromagnetic ratio. $4\pi M_s$ and $\gamma/2\pi$ values were found to be 1196.1 Oe and 2.88 MHz Oe^{-1}, respectively. The linewidth (ΔH) of the spectra was obtained by measuring the peak-to-peak distance, as shown in the inset of Fig. 2b. (ΔH was also observed to increase linearly with frequency and was analyzed using the relationship: $\Delta H = \Delta H_0 + 1.16\alpha(2\pi f/\gamma)$. Here ΔH_0 is the inhomogeneous line width and α is the gilbert damping factor which was found to be 1.72×10^{-4}. This low damping confirmed the quality of the fabricated YIG thin film and thus it can be used for spin wave propagation. The FMR response from the Py dot array on the GGG at 12 GHz showed multiple modes at a lower field region far away from the mode observed for the YIG sample. In the sample with the Py dots grown on the YIG two groups of modes were distinctly observed at 12 GHz. The high

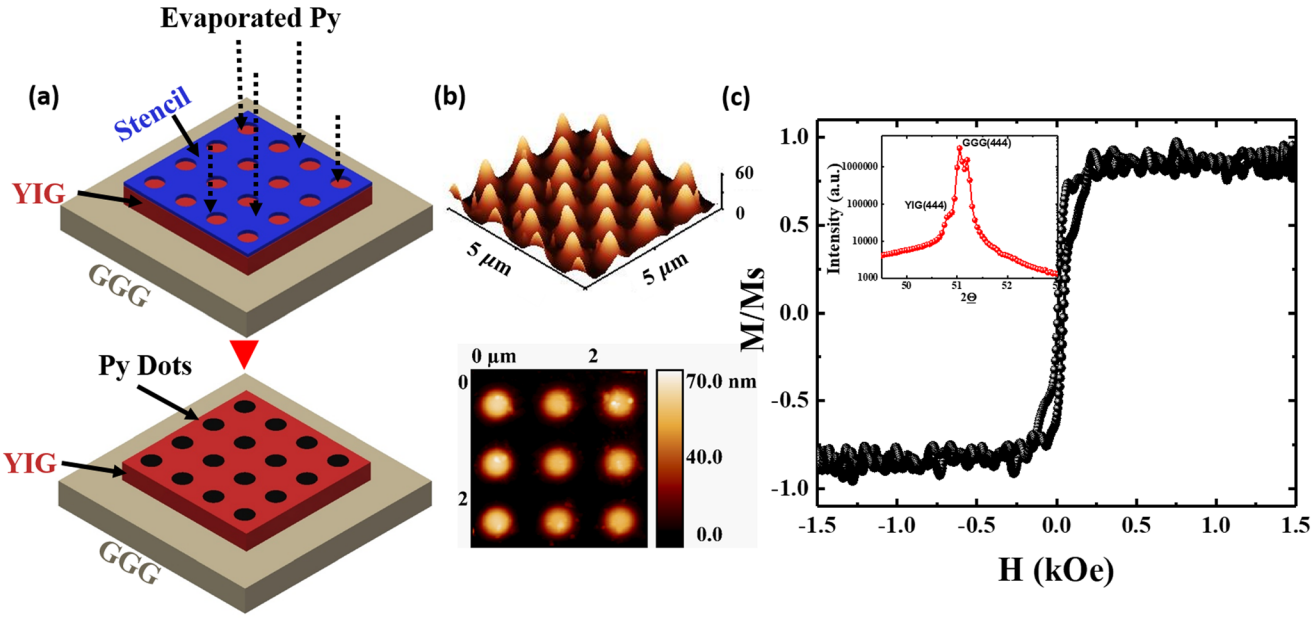

Fig. 1 (a) Schematic diagram of the deposition method. Py dots were fabricated on top of a YIG thin film grown on the GGG using a stencil membrane. (b) AFM images of the Py dots. (c) A normalized M–H loop obtained from the longitudinal MOKE setup which is in agreement with the simulated M–H loop. Inset: the XRD pattern of the continuous YIG film on the GGG.

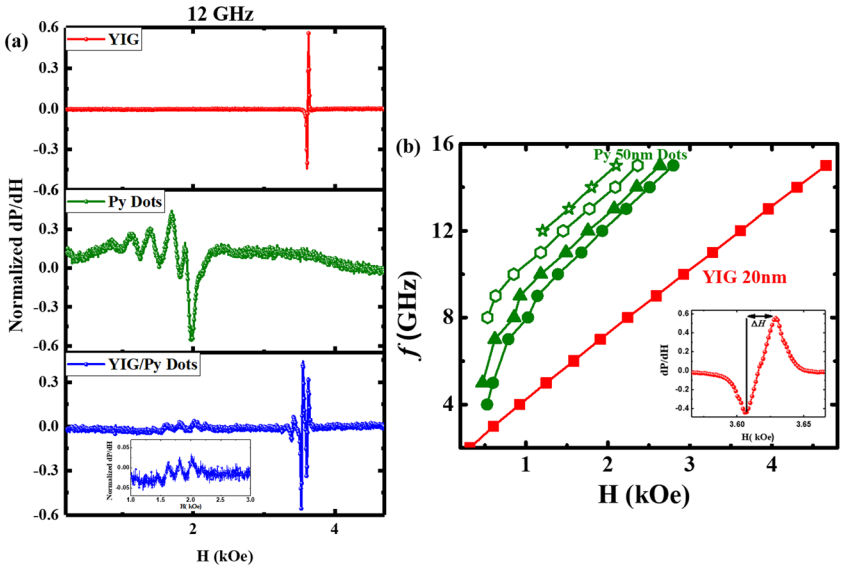

Fig. 2 (a) Resonance spectra at 12 GHz for the continuous YIG film on the GGG (top panel), Py dots deposited on the GGG (middle panel) and the YIG film (bottom panel). The inset in the bottom panel: zoomed view of the low field resonance modes. (b) The resonance frequencies corresponding to their resonance fields for the sample of the YIG continuous film (red squares) and Py dots grown on the GGG (green symbols). The solid line represents the Kittel fit of the resonance frequencies observed for the YIG continuous film. The lines joining the resonance frequencies for the Py dots are provided to identify different modes. Inset: zoomed view of the spectra obtained from the continuous YIG film at 12 GHz. The linewidth (ΔH) of resonance was taken as the peak to peak distance.

field modes displayed narrow line widths, while the low field modes were broader with lower signal strength. The signal strength for the Py dots is lower since the volume of Py contributing to the FMR signal was less than the YIG continuous film. A zoomed-in view of the low field modes is shown in the inset of Fig. 2a.

The FMR response from the sample of Py dots grown on YIG is presented as a function of the resonance frequency in Fig. 3a. Three distinct narrow modes were observed to move to higher fields as the frequency increased. Similarly, a group of broad resonance modes was observed at lower magnetic fields of 10, 12 and 15 GHz. The frequencies corresponding to the resonance fields are plotted in Fig. 3b. The modes occurring at the high field values were labeled as Y_1, Y_2, and Y_3 depending on the field value they occurred at, with Y_1 occurring at the highest field value and Y_3 occurring at the lowest field value. Similarly, the two most prominent modes occurring in the lower fields were labelled as PyD_1 and PyD_2. The FMR signals from these modes were very small as compared to the modes observed in the YIG layer and therefore, we focused primarily on the YIG modes. Comparing these modes with the modes in Fig. 2, mode Y_1 occurred around the same field as the funda-

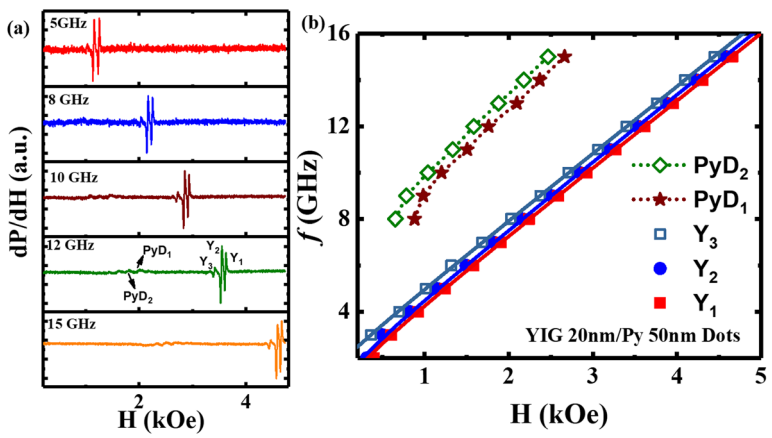

Fig. 3 (a) Resonance spectra of the sample of Py dots grown on the YIG thin film at 5, 8, 10, 12, and 15 GHz. (b). Resonance frequencies corresponding to the resonance fields for the same sample. The solid lines Y_1, Y_2, and Y_3 and the low field modes PyD_1 and PyD_2 are connected by dotted lines to aid the eye.

mental mode observed in the YIG film. At 12 GHz, the three high field modes occurred at 3396 Oe, 3538 Oe and 3615 Oe with line widths of 27 Oe, 26 Oe and 24 Oe, respectively. The FMR mode for the continuous YIG film occurred at 3613 Oe with a line width of 24 Oe. We can infer that the continuous YIG film mode is present in the YIG/Py(dots) sample and occurs along with additional modes due to the influence of the Py dots. Y_1 appears to be the mode originating from the continuous YIG film, while Y_2 and Y_3 are the distinct modes due to an increased contribution of stray fields[27] from Py dots. From the linewidth analysis, the damping parameters for the three modes Y_1, Y_2 and Y_3 were found to be $\alpha_{Y_1} = 2.31 \times 10^{-4}$, $\alpha_{Y_2} = 4.19 \times 10^{-4}$ and $\alpha_{Y_3} = 2.97 \times 10^{-3}$, respectively. The mode originating from the continuous film was able to retain a low damping parameter and the increase in damping parameters can be attributed to additional loss channels due to the coupling of spin wave modes. Thus, there was no decrease in the quality of the YIG film due to the deposition of Py using stencil lithography.

To understand the experimental results further, in Fig. 4a we present a simulated magnetization (M) *versus* field (H) curve for our fabricated YIG/Py (nanodot) sample. In the simulation, the YIG thickness was fixed at 20 nm and Py thickness was fixed at 50 nm. The Py dots were 500 nm in diameter and the edge-to-edge distance was also maintained at 500 nm (center-to-center distance was 1000 nm). The magnetization of the sample was simulated from −5 kOe to 5 kOe (presented by red dots) and from 5 kOe to −5 kOe (presented by black dots). The M–H loop is similar to the M–H loops of Py dot arrays as previously reported, investigating the vortex state (VS) in Py dots.[28,29] The magnetization in both the Py dots and the YIG layer is presented in Fig. 4b–e for −1000 Oe, 0 Oe, 600 Oe, and 1000 Oe, respectively. At −1000 Oe, the magnetic moments in the Py dots and YIG layer are saturated along the applied field direction. As the field is decreased, the magnetic moments in the Py dots relax following the circumference of the dot and a sharp decrease in magnetization corresponds to the nucleation of the VS. Due to the exchange interaction of the Py dots with the YIG film, the YIG underneath the Py dots also nucleates to form a VS. The vortex is at the center of the Py dots at 0 Oe. The VS in the YIG layer has the same polarity as that in the Py dots due to the ferromagnetic exchange coupling between the layers. As the field is further increased, the vortex core moves perpendicularly to the applied magnetic field and is annihilated when it reaches the top/bottom. The YIG region directly below the Py dots follows the magnetization states of the Py dots. Qualitatively, we observe two distinct regions in the YIG layer. One corresponds to the region underneath the Py dots which behave like YIG nanodots but follow the magnetization of Py dots, and the other region corresponds to the rest of the YIG film. There are sharp domains seen near the edge of the Py Dots on the YIG film, which can be explained by the interaction of the induced vortex magnetization in the YIG film with the surrounding magnetization in the YIG film. Further simulations were done by increasing the Py dot diameter to D = 250, 500, and 800 nm while keeping the center-to-center distance the same, and similar stray field effects were observed. The magnetic states of the Py dots were transferred to the underlying YIG films. With an increase in the diameter, the nucleation starts to occur earlier while annihilation is at higher magnetic fields, as shown in the inset of Fig. 4a. Thus, the simulations show considerable agreement with our proposal to tune a continuous YIG film to form pseudo-YIG nanostructures.

To understand the magnetization dynamics of the structure, dynamic simulations were also carried out. In the simulations, the Py dots were perfect and completely cylindrical. The simulated spectra of the structure are presented in Fig. 5a along with the simulated spectra of the Py dots, and the con-

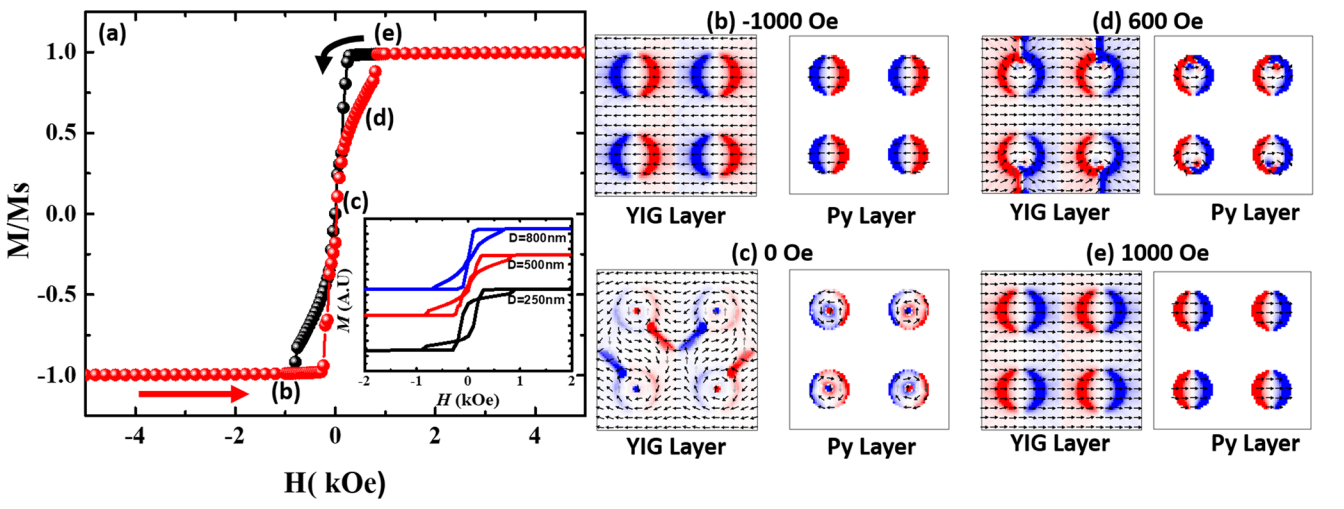

Fig. 4 (a) Simulated hysteresis loop for the sample of Py dots on YIG. The dots were placed 1000 nm (center to center distance) away from each other with a diameter D = 500 nm. The red color depicts a sweep from −5 kOe to +5 kOe and the black curve is the reverse sweep. (b)–(e) Magnetization states of the bilayer structure corresponding to the locations in the M–H loop when taken from negative saturation to positive saturation. Inset: a simulated hysteresis loop for Py dots with D = 250 nm, 500 nm and 800 nm.

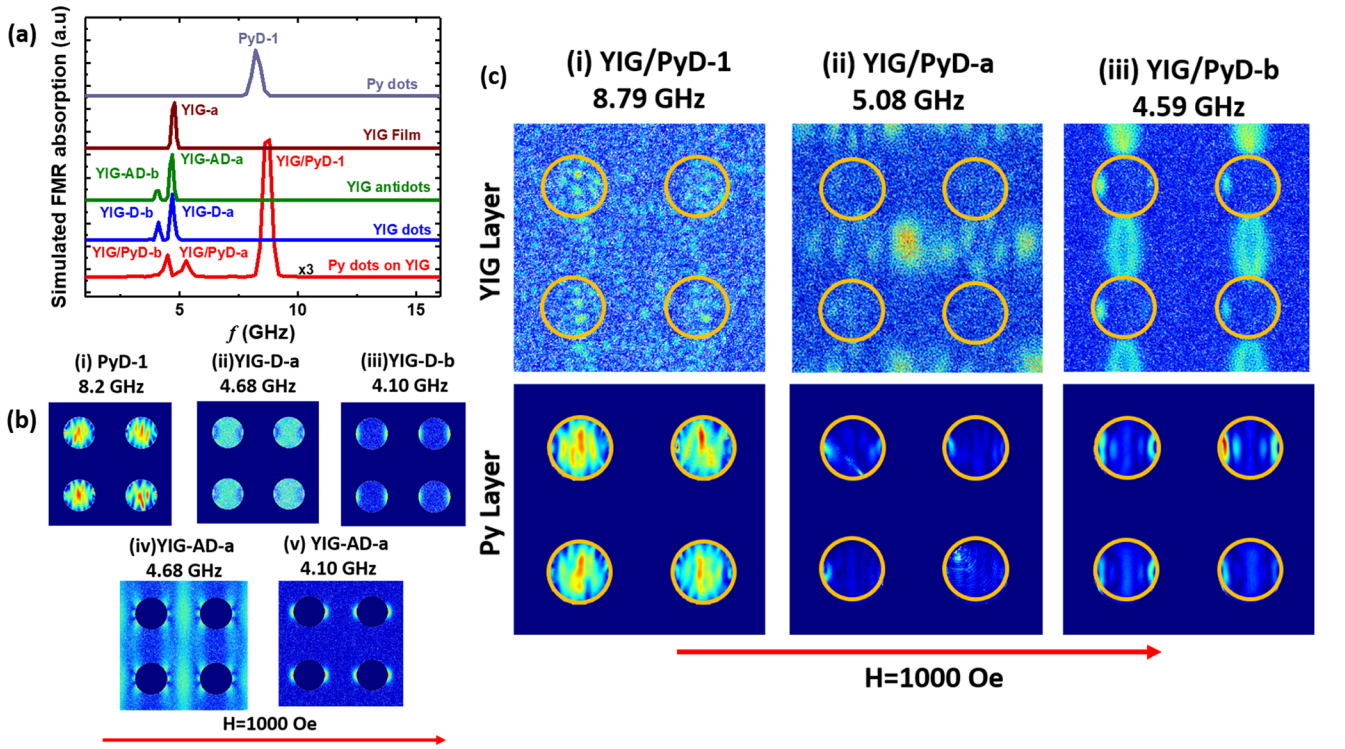

Fig. 5 (a) Simulated dynamic spectra of a sample of only Py dots (50 nm thick and 500 nm in diameter with a spacing of 1000 nm between the dots), a 20 nm thick continuous film of YIG, a sample of the YIG film with empty holes (YIG antidots), a sample of 20 nm thick YIG dots and a sample of Py dot arrays on YIG (b) (i)–(v) are the mode profiles of PyD-1, YIG-D-a, YIG-D-b, YIG-AD-a, and YIG-AD-b modes identified in the simulated dynamic spectra in the m_z direction. (c) (i)–(iii) are the mode profiles of the YIG/PyD-1, YIG/PyD-a, and YIG/PyD-b modes identified in the simulated dynamic spectra of the Py dot arrays on the YIG. The yellow circles are used to indicate the position of the Py dots on top of the YIG layer.

tinuous film of YIG, YIG dots, and YIG antidots at an applied magnetic field of 1000 Oe. The resonance modes and their corresponding mode profiles are also presented in Fig. 5b. The simulated results from Py dots as well as the YIG continuous film exhibited a single resonance mode. The resonance in the Py dots occurred at 8.20 GHz showing a central mode[30] in each dot which has been labeled as PyD-1 and the resonance for the continuous YIG film occurred at 4.78 GHz labeled as YIG-a. The simulations for the YIG antidot and YIG dot structures exhibited two resonance modes at 4.69 GHz and 4.10 GHz. Three distinct modes were observed for the combined structure of Py dots on the YIG film. Mode YIG/PyD-1 occurred at 8.79 GHz and modes YIG/PyD-a and YIG/PyD-b occurred at 5.27 GHz and 4.49 GHz, respectively. The mode profiles for these modes are given in Fig. 5c with the contours of the Py dots overlaid on the spin-wave intensity map of the YIG layer.

In mode YIG/PyD-1 occurring at 8.79 GHz, the YIG layer exhibits no distinct spin-wave mode while the Py dots on top of the YIG exhibit intense central modes similar to mode PyD-1 in the sample of only Py dots. The lower frequency modes correspond to spin-wave excitations predominantly in the YIG film. The spin wave intensity is along the applied field direction in mode YIG/PyD-a and perpendicular to the applied field in YIG/PyD-b. Compared with experimental data, Y_3 corresponds to YIG/PyD-a and Y_2 corresponds to YIG/PyD-b.

Interestingly, for both, modes YIG/PyD-a and YIG/PyD-b do not run throughout the parallel strips below the Py dots which is in contrast with what was observed by Duerr *et al.*[31] in an antidot lattice of Py with Co nanodisks. For the YIG/PyD-b mode, the spin waves are localized along the perpendicular direction of the applied magnetic field and in-between the dot contour overlays. Spin wave modes are also localized near the edges of the Py dots and can be observed in both the YIG layer and the Py layer. In the YIG layer, this is similar to the mode observed in the YIG dots (YIG-D-b). Therefore, the proposed structure has potential to show interesting properties in terms of both static and dynamic properties.

Conclusions

We have demonstrated a simple and reliable method to indirectly pattern YIG films on GGG substrates. We fabricated exchange-coupled Py dot arrays onto the underlying YIG films using nanostencil lithography. The stray field generated from the Py dot arrays is used to communicate patterned magnetic information to the underlying YIG films. For the reference YIG film, as expected, a single field-dependent resonance mode with a narrow linewidth was observed. In contrast, for a hybrid YIG/Py dot structure, three distinct YIG resonance modes were

observed as predicted by micromagnetic simulations. Thus, we have demonstrated the use of stray fields to pattern YIG films, opening up a new route for the development of future YIG-based magnonic devices.

Conflicts of interest

There are no conflicts to declare.

Acknowledgements

This work was supported by the Ministry of Education Singapore Tier 2 funding *via* grant numbers: R-263-000-C61-112 and R144-000-442-114. A. O. A and R. M are the members of the Singapore Spintronics Consortium (SG-SPIN).

References

1 M. Collet, O. Gladii, M. Evelt, V. Bessonov, L. Soumah, P. Bortolotti, S. O. Demokritov, Y. Henry, V. Cros, M. Bailleul and V. E. Demidov, Spin-wave propagation in ultra-thin YIG based waveguides, *Appl. Phys. Lett.*, 2017, **110**, 092408.

2 L. J. Cornelissen, J. Liu, R. A. Duine, J. B. Youssef and B. J. Van Wees, Long-distance transport of magnon spin information in a magnetic insulator at room temperature, *Nat. Phys.*, 2015, **11**, 1022.

3 Y. Sun, Y. Y. Song and M. Wu, Growth and ferromagnetic resonance of yttrium iron garnet thin films on metals, *Appl. Phys. Lett.*, 2012, **101**, 082405.

4 R. C. Linares, R. B. McGraw and J. B. Schroeder, Growth and Properties of Yttrium Iron Garnet Single–Crystal Films, *J. Appl. Phys.*, 1965, **36**, 2884.

5 Y. Sun, Y. Y. Song, H. Chang, M. Kabatek, M. Jantz, W. Schneider, M. Wu, H. Schultheiss and A. Hoffmann, Growth and ferromagnetic resonance properties of nanometer-thick yttrium iron garnet films, *Appl. Phys. Lett.*, 2012, **101**, 152405.

6 H. Wang, C. Du, P. C. Hammel and F. Yang, Strain-tunable magnetocrystalline anisotropy in epitaxial Y3Fe5O12 thin films, *Phys. Rev. B: Condens. Matter Mater. Phys.*, 2014, **89**, 134404.

7 T. Liu, H. Chang, V. Vlaminck, Y. Sun, M. Kabatek, A. Hoffmann, L. Deng and M. Wu, Ferromagnetic resonance of sputtered yttrium iron garnet nanometer films, *J. Appl. Phys.*, 2014, **115**, 17A501.

8 A. A. Serga, A. V. Chumak and B. Hillebrands, YIG magnonics, *J. Phys. D: Appl. Phys.*, 2010, **43**, 264002.

9 J. G. Zhu, Y. Zheng and G. A. Prinz, Ultrahigh density vertical magnetoresistive random access memory, *J. Appl. Phys.*, 2000, **87**, 6668.

10 M. M. Miller, G. A. Prinz, S. F. Cheng and S. Bounnak, Detection of a micron-sized magnetic sphere using a ring-shaped anisotropic magnetoresistance-based sensor: A model for a magnetoresistance-based biosensor, *Appl. Phys. Lett.*, 2002, **81**, 2211.

11 M. B. Jungfleisch, W. Zhang, W. Jiang, H. Chang, J. Sklenar, S. M. Wu, J. E. Pearson, A. Bhattacharya, J. B. Ketterson, M. Wu and A. Hoffmann, *J. Appl. Phys.*, 2015, **117**, 17D128.

12 W. Zhang and K. M. Krishnan, Epitaxial patterning of thin-films: conventional lithographies and beyond, *J. Micromech. Microeng.*, 2014, **24**, 093001.

13 E. N. Beginin, A. V. Sadovnikov, A. Y. Sharaevskaya, A. I. Stognij and S. A. Nikitov, Spin wave steering in three-dimensional magnonic networks, *Appl. Phys. Lett.*, 2018, **112**, 122404.

14 S. Li, W. Zhang, J. Ding, J. E. Pearson, V. Novosad and A. Hoffmann, Epitaxial patterning of nanometer-thick Y3Fe5O12 films with low magnetic damping, *Nanoscale*, 2016, **8**, 388.

15 N. Zhu, H. Chang, A. Franson, T. Liu, X. Zhang, E. Johnston-Halperin, M. Wu and H. X. Tang, Patterned growth of crystalline Y3Fe5O12 nanostructures with engineered magnetic shape anisotropy, *Appl. Phys. Lett.*, 2017, **110**, 252401.

16 Z. Xu, H. Zheng and M. Han, Preparation and morphology, magnetic properties of yttrium iron garnet nanodot arrays on Gd3Ga5O12 substrate, *Chem. Phys. Lett.*, 2017, **680**, 90.

17 G. Schmidt, C. Hauser, P. Trempler, M. Paleschke and E. T. Papaioannou, Ultra Thin Films of Yttrium Iron Garnet with Very Low Damping: A Review, *Phys. Status Solidi B*, 2020, 1900644.

18 Z. Zhang, M. Vogel, M. B. Jungfleisch, A. Hoffmann, Y. Nie and V. Novosad, Tuning edge-localized spin waves in magnetic microstripes by proximate magnetic structures, *Phys. Rev. B*, 2019, **100**, 174434.

19 Z. Zhang, M. Vogel, J. Holanda, M. B. Jungfleisch, C. Liu, Y. Li, J. E. Pearson, R. Divan, W. Zhang, A. Hoffmann and Y. Nie, Spin-wave frequency division multiplexing in an yttrium iron garnet microstripe magnetized by inhomogeneous field, *Appl. Phys. Lett.*, 2019, **115**, 232402.

20 H. Yu, O. D. A. Kelly, V. Cros, R. Bernard, P. Bortolotti, A. Anane, F. Brandl, F. Heimbach and D. Grundler, Approaching soft X-ray wavelengths in nanomagnet-based microwave technology, *Nat. Commun.*, 2016, **7**, 11255.

21 W. Bao, G. Liu, Z. Zhao, H. Zhang, D. Yan, A. Deshpande, B. LeRoy and C. N. Lau, Lithography-free fabrication of high quality substrate-supported and freestanding graphene devices, *Nano Res.*, 2010, **3**, 98.

22 L. Gross, R. R. Schlittler, G. Meyer and R. Allenspach, Magnetologic devices fabricated by nanostencil lithography, *Nanotechnology*, 2010, **21**, 325301.

23 S. Aksu, A. A. Yanik, R. Adato, A. Artar, M. Huang and H. Altug, High-throughput nanofabrication of infrared plasmonic nanoantenna arrays for vibrational nanospectroscopy, *Nano Lett.*, 2010, **10**, 2511.

24 K. Du, J. Ding, Y. Liu, I. Wathuthanthri and C. H. Choi, Stencil lithography for scalable micro-and nanomanufacturing, *Micromachines*, 2017, **8**, 131.

25 O. Vazquez-Mena, G. Villanueva, V. Savu, K. Sidler, M. A. F. Van Den Boogaart and J. Brugger, Metallic nanowires by full wafer stencil lithography, *Nano Lett.*, 2008, **8**, 3675.
26 A. Papp, W. Porod and G. Csaba, Hybrid yttrium iron garnet-ferromagnet structures for spin-wave devices, *J. Appl. Phys.*, 2015, **117**, 17E101.
27 P. Che, K. Baumgaertl, A. Kúkol'ová, C. Dubs and D. Grundler, Efficient wavelength conversion of exchange magnons below 100 nm by magnetic coplanar waveguides, *Nat. Commun.*, 2020, **11**, 1.
28 C. A. Vaz, T. J. Hayward, J. Llandro, F. Schackert, D. Morecroft, J. A. C. Bland, M. Kläui, M. Laufenberg, D. Backes, U. Rüdiger and F. J. Castaño, Ferromagnetic nanorings, *J. Phys.: Condens. Matter*, 2007, **19**, 255207.
29 P. Lupo, D. Kumar and A. O. Adeyeye, Size dependence of spin-wave modes in Ni80Fe20 nanodisks, *AIP Adv.*, 2015, **7**, 077179.
30 G. Shimon and A. O. Adeyeye, Size-dependent magnetization dynamics in individual Ni80Fe20 disk using microfocused Brillouin Light Scattering spectroscopy, *AIP Adv.*, 2015, **5**, 097124.
31 G. Duerr, M. Madami, S. Neusser, S. Tacchi, G. Gubbiotti, G. Carlotti and D. Grundler, Spatial control of spin-wave modes in Ni80Fe20 antidot lattices by embedded Co nanodisks, *Appl. Phys. Lett.*, 2011, **99**, 202502.